# Numerical Predictions of Mode Reflections in an Open Circular Duct: Comparison with Theory

Milo D. Dahl*

*NASA Glenn Research Center, Cleveland, OH, 44135, USA*

Ray Hixon†

*University of Toledo, Toledo, OH, 43606, USA*

**The NASA Broadband Aeroacoustic Stator Simulation code was used to compute the acoustic field for higher-order modes in a circular duct geometry. To test the accuracy of the results computed by the code, the duct was terminated by an open end with an infinite flange or no flange. Both open end conditions have a theoretical solution that was used to compare with the computed results. Excellent comparison for reflection matrix values was achieved after suitable refinement of the grid at the open end. The study also revealed issues with the level of the mode amplitude introduced into the acoustic field from the source boundary and the amount of reflection that occurred at the source boundary when a general nonreflecting boundary condition was applied.**

## I. Introduction

Many different sources of noise exist that may generate sound within a ducted system, a rotating fan near a fixed stator being one common example. With the ducting being finite in extent, the sound propagates along the duct toward the exit and eventually escapes out the open end to radiate into the far field. Not all of the sound escapes. Some of it reflects from the exit location back into the ducted system. At low frequencies where the wavelengths are large compared to the duct radius, acoustic plane waves propagate. The lowest frequency waves completely reflect at the opening and as the frequency increases, more of the incident sound propagates out the duct. With increasing frequency and shorter wavelengths, the sound begins to bounce around inside the duct making patterns, called modes, in the sound field across the duct area containing nodes and anti-nodes. The shape of the modes depends on the duct cross-sectional area shape and the complexity of the modal pattern increases with frequency. A particular mode may exist or propagate in a duct above a certain frequency known as the cut-off frequency. At frequencies less than the cut-off frequency, the mode cannot propagate and decays rapidly with distance along the duct axis. When a mode propagating at a frequency higher than its cut-off frequency reaches an open end, it tends to readily radiate outward. Many of these duct mode characteristics have been described mathematically.

The computation of duct modes using closed-form mathematical functions such as those for rectangular and circular ducts is well known.[1] The formulas clearly identify those modes that propagate within the duct and those modes that are cut-off and do not propagate. When a propagating mode encounters an open duct end, the mathematical analysis required to predict what happens to the mode, its reflection back into the duct, its scattering into other modes, and its transmission outward from the duct into the free space, becomes complicated and depends on the geometry of the duct termination. A duct terminating in a large wall or flange that extends outward over a great number of wavelengths is analyzed in the classical works of Rayleigh[2] and of Morse.[3] Though different approaches have been used, see for example Norris & Sheng,[4] they all tend to initially follow the approach of Zorumski[5] for the generalized solution for any mode incident on the open end of a flanged duct. Zorumski derived an equation for the reflection matrix that includes the reflection coefficient for the incident propagating mode that reflects into the same mode propagating in

*Senior Research Scientist, Acoustics Branch, Senior Member AIAA

†Associate Professor, Senior Member AIAA

the opposite direction and the conversion coefficients of the incident mode into any other propagating and non-propagating modes in the opposite direction. While complicated, the solution for mode reflection at the open end of a flanged duct is simpler than that required for the solution at the open end of an unflanged (thin) duct. The case of the incident plane wave was analyzed by Levine & Schwinger[6] for an unflanged, circular duct. Subsequent analysis by Lansing et al.[7] and by Rienstra[8] present reflection and conversion coefficients for all incident modes in circular ducts, as well as annular ducts, and add the effects of a mean flow. A generalization of the duct exit conditions using hyperboloid shapes has been explored by Cho.[9] In these studies using unflanged ducts, the walls of the duct are infinitely thin. Ando[10] provides a solution for the reflection of a plane wave at the open end of a circular duct with wall thickness.

Numerical calculations are required to solve the integrals inherent in the analytical solutions obtained for open end ducts with circular geometries. For complicated geometries and the general inclusion of mean flow effects, computational aeroacoustics (CAA) techniques are applied to solve for the propagation and attenuation of sound in ducts and the radiation of sound to the far field.[11–13] Examples of techniques using various finite difference approaches are found in the proceedings for the Second CAA Workshop on Benchmark Problems.[14] In that proceedings, the Category 2 problems are related to the calculation of sound propagating within ducts. The second problem in the category specifies for a given source that the propagating sound be computed within a duct and the directivity of the sound radiated from the open end be computed in the far field. In solving the problem, the circular duct geometry was made part of the grid system both internal and external to the duct. A source was defined within the duct and radiation boundary conditions were applied outside the duct. Any reflection at the duct end was expected to naturally occur though calculation of the reflection coefficients were not specified as part of the problem statement. Samples of the computed pressure field within the duct showed the presence of standing waves indicative of reflections from the open end. For the solutions given in the proceedings, there was a 43 percent difference between the solution with the largest standing wave and the solution with the smallest standing wave. Evidently there were issues with the solutions within the interior of the grid where reflections were generated at the duct open end.

Finite elements are another CAA technique applied to solving for sound propagation in and radiation from ducts.[11] This method can easily be applied to ducts with simple geometries (i.e. circular) and to ducts with more complicated geometries such as with varying area. The method can be set up for a known set of modes propagating toward the open duct end. Then within the duct, the method solves for both the mode shapes, estimated using finite element basis functions, and the reflected mode amplitudes. Reflection coefficients are then computed. Examples of using this approach are found in Astley,[15] Meyer,[16] and Nallasamy et al.[17] Astley found excellent comparison of the finite element code computed reflection coefficients with results from an analytical solution.[9] The latter two publications present results for reflection coefficients with various changes in geometry, frequency, mode shape, and flow speed. No comparisons were made to results from analytical solutions or measured data.

In a previous study, Dahl et al.[18] compared reflection coefficients determined from in-duct measurements with those determined from numerical code calculations. The preliminary results did not agree and further investigation was suggested to determine the accuracy of both the measured results and the computed results. In this paper, the accuracy of the numerical code to calculate the propagation and reflection of higher-order modes in a circular duct with an open end is explored. The issues affecting the numerical calculations to be discussed are the input boundary condition and the grid spacing near the open end of the duct. The accuracy of the results was determined by post-processing the numerical data, computing reflection coefficients, and comparing those to reflection coefficients computed from the analytical theories found in Zorumski[5] and Rienstra.[8] To study the input boundary, calculations were performed using a simple closed end duct geometry with and without a damping layer at the end opposite the source. The results revealed how well the numerics introduced the source conditions into the field domain within the duct and how much acoustic energy propagating within the duct was reflected rather than absorbed by the inflow boundary condition at the source end of the duct.

## II. Numerical Solution of the Governing Equations

Numerical calculations were performed using the NASA Glenn Broadband Aeroacoustic Stator Simulation (BASS) code. This code is an unsteady CAA code that uses explicit fourth-order time marching schemes combined with high-order spatial differencing schemes to accurately solve the unsteady nonlinear Euler or

Navier-Stokes equations.[19–24] Using a finite-difference time-domain approach, the BASS code solves these equations in chain-rule, curvilinear form. For topological flexibility, the code uses structured multiblock grids. BASS is written in standard Fortran 2008 for portability and maintainability and is parallelized using the MPI-2 standard.[25] BASS has been tested on a range of compilers and MPI implementations, and has been validated on a number of benchmark aeroacoustics problems.

The BASS code has a number of spatial differencing schemes, artificial dissipation methods, and explicit time marching schemes implemented. For this work, the BASS code was run using the HALE-RK67 time marching scheme.[26] An automatic shock-capturing dissipation model[27] was used, based on the explicit filters of Kennedy and Carpenter.[28] The Tam and Webb 7-point optimized fourth-order DRP scheme was used for the spatial differencing.[29] The nonreflecting boundary conditions of Giles[30] were used at the driver and far-field boundaries, combined with a source term used to impose acoustic modes at the driver boundary.

## III. Computational Details

The computational domain has a far-field boundary outside the duct, continues into the duct and has another boundary at the acoustic driver location inside the duct. The incoming acoustic modes are imposed at this boundary. The Giles[30] nonreflecting boundary condition is used to allow outgoing waves to exit the computational domain with minimal reflection.

For all cases, a reference grid is generated using the GridPro/az3000 grid generator.[31] This reference grid has a duct wall of zero thickness. A representative acoustic field solution using this grid, referred to as the unflanged or thin duct, is shown in Figure 1a. The duct wall is made thicker by removing grid blocks from the reference grid. Figure 1b shows an example acoustic field for a thicker walled duct with a wall thickness of $0.28R$, where $R = 24\,\text{inches}$ (0.61 m) is the duct radius. This duct is labeled the 'medium' flanged duct. The last part, Figure 1c, shows an example acoustic field for the infinite flanged duct. In all cases, the duct length is 100 inches (2.54 m). The grids have a minimum of 10 grid points per wavelength of the highest-frequency acoustic modes, which is well within the resolution capabilities of the DRP scheme. The grid is clustered radially and axially around the duct exit as shown in Figure 2. The acoustic source location is at the right end in this figure and the sound propagates toward the open end with the infinite flange on the left.

## IV. Numerical Data Post-Processing

The numerical solution generated by the BASS code contains transients during the initial phase of the calculations. Once this phase has passed, the numerical solution was the steady state acoustic field generated by the source located at the driver boundary. Now, as each time step was taken in the calculations, each spatial grid in the field provided a time history of the acoustic field at that point. These data were processed to determine the acoustic modes in the duct including mode amplitude and direction of propagation.

The unsteady solution was desired at particular locations on cross-sectional planes perpendicular to the axis in the acoustic field within the circular duct. Specifically, nine axial locations were chosen. At each axial location, 31 radial points were chosen on the planar surface and at each radius, there were 64 uniformly-spaced, azimuthal points. Bilinear interpolation, as necessary, was applied to the unsteady flow data to obtain the solution at these locations.

The acoustic field in the duct may be represented analytically as a combination of acoustic modes

$$p(x,r,\theta,t) = \Re\left\{\sum_{s}\sum_{m=-M}^{M} C_m^s(x,r)e^{-j2\pi f_s t}e^{jm\theta}\right\} \tag{1}$$

where $p$ is the real acoustic pressure that is shown to be a cyclical function of time $t$ and the azimuthal direction $\theta$ since in a circular duct, the pressure must be repetitive in that direction. It is also shown to be a general summation of spatial modes $C_m^s(x,r)$ over all existing frequencies $f_s$ and circumferential mode indices $m$. To begin to extract the modal information from the computed acoustic pressure, a discrete Fourier transform

$$\hat{P}(\ell) = \frac{1}{K}\sum_{k=0}^{K-1} p(k)e^{j2\pi\ell k/K} \qquad \ell = 0,1,2,\ldots,K-1 \tag{2}$$

was performed on $p(k)$, the discrete samples of the time history at each spatial location. With the acoustic source generating sound at a particular frequency, the discrete time history form of equation (1) for the acoustic pressure at a single frequency and at a particular spatial location becomes

$$p(x_1, r_i, \theta_\nu, k) = \Re\left\{ \sum_{m=-M}^{M} C_m^s(x_1, r_i) e^{-j2\pi sk/K} e^{jm\theta_\nu} \right\} \tag{3}$$
$$t = k\Delta t \qquad k = 0, 1, 2, \ldots, K-1$$

The now single, source frequency $f_s$ is related to the frequency increment $\Delta f$ according to

$$f_s = s\Delta f$$

where $\Delta f^{-1} = K\Delta t$ and the variable $s$ is, in general, not necessarily an integer. Performing the transform on equation (3) gives

$$\hat{P}(x_1, r_i, \theta_\nu, \ell) = \frac{1}{2} \sum_{m=-M}^{M} C_m^s(x_1, r_i) e^{jm\theta_\nu} h(s-\ell) + \frac{1}{2} \sum_{m=-M}^{M} C_m^{s*}(x_1, r_i) e^{-jm\theta_\nu} h(K-s-\ell) \tag{4}$$

where $h$ is a function that accounts for spectral leakage if $s$ is not an integer. The second term on the right side of equation (4) is the complex conjugate of the first term. The time histories are $K = 32$ points long over two periods of data with the source generator set to $f_s = 960\,\text{Hz}$. Thus, $f_s = K\Delta t/2$ resulting in $s = f_s/\Delta f = 2$, an integer, and $h \to \delta$ a unit delta function at $\ell = s$ and is zero otherwise. The data at this frequency was identified in the transformed results and stored for the next step.

A spatial transform is now performed on the $N_\theta = 64$ points in the azimuthal direction obtained for the amplitude data from equation (4) at $\ell = 2$ at a particular radial and axial location. The spatial discrete Fourier transform is

$$P(\mu) = \frac{1}{N_\theta} \sum_{\nu=0}^{N_\theta - 1} \hat{P}(\nu) e^{-j2\pi\mu\nu/N_\theta} \qquad \mu = 0, 1, 2, \ldots, N_\theta - 1 \tag{5}$$

Writing the discrete version of equation (4) using $\theta_\nu = 2\pi\nu/N_\theta$, for the data points at $\ell = 2$ as

$$\hat{P}(x_1, r_i, \nu, \ell) = \frac{1}{2} \sum_{m=0}^{M} C_m^\ell(x_1, r_i) e^{j2\pi m\nu/N_\theta} + \frac{1}{2} \sum_{m=M}^{1} C_{-m}^\ell(x_1, r_i) e^{-j2\pi m\nu/N_\theta} \tag{6}$$
$$\nu = 0, 1, 2, \ldots, N_\theta - 1$$

Substitute into equation (5) and reduce to the form

$$P(x_1, r_i, \mu, \ell) = \frac{1}{2} \sum_{m=0}^{M} C_m^\ell(x_1, r_i) \delta(m-\mu) + \frac{1}{2} \sum_{m=M}^{1} C_{-m}^\ell(x_1, r_i) \delta(N_\theta - m - \mu) \tag{7}$$

The outputs of this spatial transform are the complex acoustic pressure amplitudes for the circumferential mode at the radial, $r_i$, and axial, $x_1$, locations. For circumferential modes that exist in the duct with $m \geq 0$, their amplitudes will appear in the first term on the right side at $\mu = m$. The amplitude values for any circumferential mode with $m < 0$ will appear in the second term at $\mu = N_\theta - m$. (Note that a positive integer $m$ is used in this term.)

The amplitude data as a function of radius at each axial location were processed in the manner described in Dahl et al.[18] to obtain the separate radial and circumferential mode amplitudes. The $x$-axis is located on the centerline of the duct with $x = 0$ located at the end of the duct and the positive direction of the $x$-axis points outward from the duct away from the source. If it is first assumed that the modes propagate in only one direction, then the amplitude $C_m^\ell(x_1, r_i)$ at each radial measurement location $r_i$ and location $x_1$ may be further decomposed into a sum of radial basis functions as

$$C_m^\ell(x_1, r_i) = \sum_{n=0}^{N_{max}-1} P_{\ell mn} E_{\ell mn}(r_i; x_1) \qquad i = 1, 2, \ldots, N_1 \tag{8}$$

where $N_1$ is the number of radial measurement points and $N_{max}$ is the number of radial mode shapes. The mode amplitudes $P_{\ell mn}$ will be constant with variations in $x_1$ if modes propagate in only one direction. Otherwise, if modes are propagating in both directions within the duct, then $P_{\ell mn}$ will be the local amplitude of the resulting standing wave. To separate the propagation direction for the radial and circumferential mode amplitudes, the amplitude at each axial location is determined from the sum of $+x$-direction and $-x$-direction propagating modes plus the inclusion of any evanescent modes. To extract the radial mode amplitudes, the numerically computed acoustic pressure amplitudes obtained from equation (7) are written as the sum of radial basis functions as follows:

$$\begin{aligned} C_m^\ell(x_1, r_i) &= \sum_{n=0}^{N_{max}-1} \left[ \left\{ P_{\ell mn}^+ e^{jk_1^+ x_1} \right\} E_{\ell mn}^+(r_i; x_1) + \left\{ P_{\ell mn}^- e^{jk_2^- x_2} \right\} E_{\ell mn}^-(r_i; x_1) e^{j(k_1^- x_1 - k_2^- x_2)} \right] \\ C_m^\ell(x_2, r'_{i'}) e^{-jm\psi} &= \sum_{n=0}^{N_{max}-1} \left[ \left\{ P_{\ell mn}^+ e^{jk_1^+ x_1} \right\} E_{\ell mn}^+(r'_{i'}; x_2) e^{j(k_2^+ x_2 - k_1^+ x_1)} + \left\{ P_{\ell mn}^- e^{jk_2^- x_2} \right\} E_{\ell mn}^-(r'_{i'}; x_2) \right] \quad (9) \\ & \qquad i = 1, 2, \ldots, N_1 \qquad i' = 1, 2, \ldots, N_2 \end{aligned}$$

where $\psi$ is any potential azimuthal offset between the data at $x_1$ and the data at $x_2$. The axial wave numbers $k$ are shown with a sign superscript to indicate the direction of propagation or decay and the subscripts '1' and '2' apply for the solution of the eigenvalue problem at the locations $x_1$ and $x_2$ which, in general, can be different if mean flow or slight area changes were present. Other indices for the axial wave number not shown in equation (9) are used to indicate that the wave number is a function of frequency, denoted by the index $\ell$, the circumferential mode number $m$, and the radial mode number $n$. Also, $r_i$ and $r'_{i'}$ denote that radial locations of the numerical data at the two axial locations may differ in location and number. This formulation rescales the amplitudes and radial basis functions to properly handle evanescent modes.

For a constant area, circular duct with no flow, the radial basis functions become only a function of radius and may be determined from the closed-form solution as

$$E_{\ell mn}^+(r) = E_{\ell mn}^-(r) = \sqrt{\mathcal{N}_m^2} \mathrm{J}_m(\kappa_{\ell mn} r) \quad (10)$$

where $\mathrm{J}_m$ is a cylindrical Bessel function of the first kind and the factor $\mathcal{N}$ is used to normalize the Bessel function and ensures that the integral of $E^2$ across the area of the duct equals the duct cross-sectional area. In addition, the axial wave numbers become

$$k_{\ell mn}^+ = -k_{\ell mn}^- = k_{\ell mn}$$

and the radial eigenvalue is related to $k$ by

$$\kappa_{\ell mn}^2 = \left( \frac{2\pi \ell \Delta f}{\mathrm{c}} \right)^2 - k_{\ell mn}^2 \quad (11)$$

where c is the average speed of sound value across the duct cross-sectional area. However, as described in Dahl et al.,[18] numerical computations were performed to get the axial wave numbers and the radial basis functions with results equivalent to the closed-form solution.

The complex radial mode amplitude solutions to equations (8) and (9) are obtained using the least-squares method. The solution is to minimize the residual sum of squares

$$e = \|\mathbf{c} - \mathbf{B}\mathbf{P}\|_2^2 \quad (12)$$

where $\mathbf{c}$ is a vector of length $n_p$ for the complex acoustc pressure amplitude data from the left side of equation (8), $n_p = N_1$, or equation (9), $n_p = N_1 + N_2$. The solution vector $\mathbf{P}$ of length $n_c$ contains the complex radial mode amplitudes $P_{\ell mn}$ from equation (8) with $n_c = N_{max}$ or the terms within braces in equation (9), $n_c = 2N_{max}$, that result in the $P_{\ell mn}^+$ and $P_{\ell mn}^-$ complex amplitudes. The matrix $\mathbf{B}$ is for the remaining coefficients in equations (8) and (9) of size $n_p \times n_c$. By ensuring that the number of radial data points totaling $n_p$ is greater than the number of radial basis functions represented by $n_c$, the problem is overdetermined and the solution is easily computed using the singular value decomposition method. See Dahl et al.[18] and Dahl & Sutliff[32] for complete details.

# V. Results

The BASS code computed the acoustic field generated by a source at one end of the duct. At the opposite end of the duct, both open end and closed end conditions were considered. The computed results from the open end duct conditions were used to test the accuracy of the computations by comparing the reflection matrix results determined from the computed data with results from analytical theory. The closed end duct computed data were used to determine the behavior of the boundary condition at the source end of the duct.

## V.A. Open End Duct

The acoustic field was computed for the sound propagating toward the open end for each of the three open end duct geometries shown in Figure 1. The source was a single acoustic mode imposed on the cross-sectional plane at the boundary. The shape of the mode for the acoustic pressure was given by equation (10) with an amplitude $P^s_{mn} = 1.4186\,\text{Pa}$ for the desired $(m, n)$ mode. ($1.4186\,\text{Pa}$ is equivalent to a nondimensional pressure of $10^{-5}$ at standard day conditions.) The acoustic velocities at the source were determined from the solution to the momentum equations. Figure 3 shows results from the post-processing technique to obtain the acoustic pressure mode amplitudes for both the single-point analysis, equation (8), and the two-point analysis to separate mode propagation direction, equation (9). The open end of the duct is located at $x/R = 0$ and the positive direction of the $x$-axis points outward from the duct. A reference point for the data analysis is at $x/R = -0.2$ and the single-point mode amplitude for this location is shown by the isolated blue symbol. Single-point analysis results are shown in green for the other eight locations along the $x$-axis. These single-point results show a portion of the standing wave generated by the incident and reflected modes to and from the open end of the duct. Taking each variable point and the reference point, a two-point analysis was performed to extract the $+x$- and $-x$-direction propagating mode amplitudes. These results are also plotted in the figure. For the results in Figures 3a and 3b, the grid was clustered near the wall and near the open end using the discretization labeled as the 'coarse' grid in Table 1. This grid did not provide sufficient spatial resolution in computing the acoustic field interactions that occur near the open end. The mode amplitudes for both the $+x$-direction and $-x$-direction propagating modes are varying in the direction of propagation when a constant amplitude was physically expected. To improve spatial resolution, a 'medium' grid was generated. The effect of this increased clustering on the computed propagating mode amplitudes is shown in Figures 3c and 3d. For the (2,0) mode incident on the open end, Figure 3c shows that the $+x$-direction incident mode amplitude was about constant as a function of axial distance and that only small differences occur in the level of the reflected mode amplitude when comparing the results with the three different open end conditions. Much larger variations in the reflected mode amplitudes occur for the incident (2,2) mode as shown in Figure 3d.

Table 1: Identification for grid clustering near the open end of the duct.

| Name | $\Delta r/R$ | $\Delta x/R$ |
|---|---|---|
| coarse | 0.0145 | 0.0417 |
| medium | 0.00675 | 0.00754 |
| fine | 0.00428 | 0.002253 |

Figure 3d also illustrates the possible effects of two numerical issues. At the input boundary, propagating acoustic modes with constant amplitudes were introduced to the numerical calculations. The $+x$-direction propagating mode amplitudes are different for each of the open end configurations when they should be the same within any small numerical uncertainty as shown in Figure 3c for the $(2, 0)$ mode. This may indicate that reflections are returning into the computational domain from the input boundary condition. Secondly, no physical dissipation was included in the governing equations and numerical dissipation was minimized; hence, the propagating mode amplitudes should be constant along the duct. The $+x$- and $-x$-direction propagating mode amplitudes in Figure 3d are varying slightly in the axial direction. This may be due to a lack of convergence in time of the solution to a steady state before data were collected for post-processing. The latter issue was considered by extending the computational time by 50% more from that of the original 'medium' grid solution. The mode amplitude results for the $(2, 2)$ mode input are shown in Figure 4a. Some

decrease in mode amplitude variations with axial location was found. A further improvement was sought by further clustering the grid near the open end using the 'fine' grid listed in Table 1. Figure 4b shows the $(2,2)$ mode amplitude results for the three open end conditions. The $+x$-direction mode amplitudes are in close agreement with slight differences in the reflected mode amplitude. These results were used to compute the reflection coefficients that are compared to reflection coefficients derived from theoretical analysis.

The post-processing of the numerically generated acoustic field in the duct produced the amplitudes for the modes propagating in each direction within the duct. A single propagating mode was generated by the source. As the mode interacts with the open end, energy was reflected back into the duct with the same mode shape. To match the boundary conditions at the open end where some energy was reflected back into the duct and the remainder radiated outward from the open end, some energy was converted into other modes of the same circumferential order. If these modes are not cut off, they will propagate away from the open end and back toward the source. The coefficients of reflection and conversion were computed from the post-processed numerical data by dividing the $-x$-direction propagating mode amplitudes by the amplitude of the single $+x$-direction propagating mode. These results were compared to results from theoretical calculations. Figure 5 shows reflection and conversion coefficients determined from the computed data shown in Figures 3 and 4 for different grids for an open duct with an infinite flange compared with the results computed from the theory by Zorumski[5] for each of the three indicated single incident modes (2,0), (2,1), and (2,2). These three modes propagate in the duct. All other modes are cut off and decay rapidly if generated.

Since the reflection and conversion coefficients were determined from mode amplitudes relative to the same incident mode amplitude, the lower computed values shown in Figure 5a were due to insufficient spatial grid resolution at the open end to properly handle the energy transfer between the interacting modes. The 90 degree corner where the duct wall meets the infinite flange creates a grid singularity resulting in first-order accuracy in the numerical solution.[33] The effect of increased clustering on the calculation of reflection and conversion coefficients from the numerical data is shown in Figures 5b and 5d. As can be seen, as the clustered grid spacing is made smaller, the computed reflection and conversion coefficients from the BASS computed data are much closer to the theoretical results. The results show that it was easier to resolve the $(2,0)$ and $(2,1)$ modes upon reflection or conversion from any incident mode. These modes have less radial variation than the $(2,2)$ mode. The open end singularity causes more difficulty in accurately computing the $(2,2)$ mode at the point of reflection or conversion from any incident mode.

Table 2: Amplitudes for $+x$- and $-x$-direction propagating modes within a duct with an infinite-flanged open end and comparison of reflection and conversion coefficients from BASS computed data with theory.

| Source mode | $(m,q)=(2,0)$ | | | $(m,q)=(2,1)$ | | | $(m,q)=(2,2)$ | | |
|---|---|---|---|---|---|---|---|---|---|
| $(m,n)$ | $(2,0)$ | $(2,1)$ | $(2,2)$ | $(2,0)$ | $(2,1)$ | $(2,2)$ | $(2,0)$ | $(2,1)$ | $(2,2)$ |
| $\lvert P^+_{mn}\rvert$[a] | 1.4219 | 0.0121 | 0.1146 | 0.0039 | 1.4047 | 0.1120 | 0.0032 | 0.0137 | 1.3987 |
| $\lvert P^-_{mn}\rvert$ | 0.1071 | 0.1115 | 0.2721 | 0.0902 | 0.0952 | 0.2367 | 0.1094 | 0.1203 | 0.3553 |
| $\lvert P^+_{mn}\rvert\lvert\Gamma^Z_{mnn}\rvert$ | 0.1074 | 0.0008 | 0.0286 | 0.0003 | 0.0952 | 0.0279 | 0.0002 | 0.0009 | 0.3488 |
| $\lvert\Gamma_{mnq}\rvert = \lvert P^-_{mn}\rvert/\lvert P^+_{mq}\rvert$ | 0.0753 | 0.0784 | 0.1914 | 0.0642 | 0.0678 | 0.1685 | 0.0782 | 0.0860 | 0.2540 |
| $\lvert\Gamma^Z_{mnq}\rvert$[b] | 0.0755 | 0.0786 | 0.1926 | 0.0643 | 0.0678 | 0.1727 | 0.0775 | 0.0850 | 0.2494 |
| Difference | −0.2% | −0.2% | −0.6% | −0.1% | −0.1% | −2.4% | 0.9% | 1.2% | 1.9% |

[a] Amplitudes $P$ are in Pa.

[b] Reflection matrix from theory by Zorumski.[5]

To consider the 'fine'-grid numerical results in more detail, the mode amplitudes and the reflection and conversion coefficients related to the infinite flange results in Figure 5d are shown in Table 2. A single mode was imposed at the source boundary to propagate in the $+x$ direction with amplitude $P^s_{mn} = 1.4186\,\text{Pa}$. This generated mode is shown to dominate the $+x$-direction propagating modes. However, two other modes other than the generated mode may propagate at the selected frequency of the source and the start of the numerical calculations may excite these modes as well. The results show that the other two $+x$-direction propagating modes exist but have amplitudes at least one order of magnitude smaller than the desired dominant single propagating mode incident upon the open end. The $-x$-direction propagating mode amplitudes $P^-$ were determined from the numerical data. They show that $|P^-_{20}|$ and $|P^-_{21}|$ are comparable in level and always

less that the $|P_{22}^-|$ amplitude. Given that there is some energy in each of the three $+x$-direction propagating modes, the value $|P_{mn}^+||\Gamma_{mnn}^Z|$, where $\Gamma_{mnn}^Z$ is the theoretical reflection coefficient for incident and reflected $(m,n)$ modes,[5] shows that the only significant reflected energy is in the same mode as the incident mode. The other two $-x$-direction reflected mode amplitudes have an order or more magnitude less than the $P^-$ mode amplitudes generated through conversion from the incident mode. Thus, the $P^-$ mode amplitudes are all due to reflection of or conversion from the single incident mode. The reflection and conversion coefficient $\Gamma_{mnq}$ computed from the numerical data is compared to $\Gamma_{mnq}^Z$ computed from the theory.[5] The difference is shown to be less than 3% where the minus sign indicates that $|\Gamma_{mnq}| < |\Gamma_{mnq}^Z|$.

Similar results are shown in Figure 6 for the unflanged, open duct condition. Here, the reflection and conversion coefficients from the Rienstra[8] theory are given for comparison. In general, it was more difficult to resolve the solution near the unflanged (thin) duct open end. The reflection and conversion coefficients determined from the BASS computed data are less accurate at the same grid resolution compared with the infinite flange results. Details from the 'fine'-grid results are shown in Table 3. Compared to the infinite flange results shown in Table 2, the dominant $+x$-direction mode amplitude incident upon the open end are all about the same. All the other mode amplitudes are higher due to higher levels of mode reflection and conversion from the unflanged duct open end. Nonetheless, even though the differences in the computed and theoretical reflection matrix values are all higher than those for the infinite flange, they are all less than about 4% using the 'fine' grid.

Table 3: Amplitudes for $+x$- and $-x$-direction propagating modes within a duct with an unflanged open end and comparison of reflection and conversion coefficients from BASS computed data with theory.

| Source mode | $(m,q)=(2,0)$ | | | $(m,q)=(2,1)$ | | | $(m,q)=(2,2)$ | | |
|---|---|---|---|---|---|---|---|---|---|
| $(m,n)$ | $(2,0)$ | $(2,1)$ | $(2,2)$ | $(2,0)$ | $(2,1)$ | $(2,2)$ | $(2,0)$ | $(2,1)$ | $(2,2)$ |
| $\lvert P_{mn}^+\rvert$[a] | 1.4215 | 0.0164 | 0.1523 | 0.0034 | 1.4025 | 0.1362 | 0.0030 | 0.0176 | 1.3947 |
| $\lvert P_{mn}^-\rvert$ | 0.1348 | 0.1395 | 0.3328 | 0.1140 | 0.1183 | 0.2938 | 0.1340 | 0.1450 | 0.4038 |
| $\lvert P_{mn}^+\rvert\lvert\Gamma_{mnn}^R\rvert$ | 0.1404 | 0.0014 | 0.0449 | 0.0003 | 0.1217 | 0.0402 | 0.0003 | 0.0015 | 0.4113 |
| $\lvert\Gamma_{mnq}\rvert = \lvert P_{mn}^-\rvert/\lvert P_{mq}^+\rvert$ | 0.0948 | 0.0981 | 0.2341 | 0.0812 | 0.0843 | 0.2095 | 0.0961 | 0.1040 | 0.2895 |
| $\lvert\Gamma_{mnq}^R\rvert$[b] | 0.0988 | 0.1019 | 0.2434 | 0.0833 | 0.0868 | 0.2144 | 0.0980 | 0.1056 | 0.2949 |
| Difference | −4.0% | −3.7% | −3.8% | −2.4% | −2.8% | −2.3% | −2.0% | −1.5% | −1.8% |

[a] Amplitudes $P$ are in Pa.

[b] Reflection matrix from theory by Rienstra.[8]

Lastly, Figure 7 shows reflection coefficients from BASS computed data using the three single incident modes for the three open end configurations. There is no theoretical result for the reflection coefficient when non-plane-wave modes are incident upon the open end of the 'medium' flange duct. It was expected that the infinite flange and the unflanged duct reflection coefficients would be limiting values and that the 'medium' flange duct would have reflection coefficients for these modes that lie in between the limiting values. The results in Figure 7 support this expectation.

### V.B. Input Boundary Condition

As discussed above, the incoming acoustic modes were imposed at the closed end boundary of the duct and at the same location the Giles[30] nonreflecting boundary condition was applied with the intent to allow waves returning toward the source to exit the computational domain. Specifically, the Giles inflow boundary condition was implemented. Table 2 shows an example of the amplitudes for modes propagating within an open end duct with an infinite flange. The imposed single mode amplitude, $P_{mn}^s = 1.4186\,\text{Pa}$, was expected to be the $+x$-direction mode amplitude incident upon the open end under ideal conditions for the imposed source mode and no reflections from the source plane. The $|P_{20}^+|$ and $|P_{21}^+|$ mode amplitudes were close to the source amplitude, but $|P_{22}^+|$ appeared to be noticeably lower. This could be due to how well the source mode was imposed at the boundary or the interference by the reflection of sound from the input nonreflecting boundary or both. Two tests were conducted to help identify the computed behavior of the sound field at the source input location. In one test, the source mode was imposed into a long duct with a damping layer at the

opposite end to prevent reflections. Thus, the amplitude of the $+x$-direction propagating mode generated by the source mode could be identified. The second test placed the Giles inflow boundary condition at the exit to determine the level of reflection created by the boundary condition. This boundary condition is known to work well for plane waves at normal incidence but increasingly reflects acoustic energy as the angle of incidence of the incoming wave increases.[34] The higher-order, propagating modes imposed by the source have wavefronts that propagate at an angle away from the axial direction and bounce off the walls of the duct. These wavefronts impact the boundary at an angle of incidence and thus some of the sound will reflect off the boundary.

To identify the mode imposed by the source, the duct was lengthened to 550 inches (14 m) with a damping layer at the end of the duct. With the origin of the $x$-axis at $x/R = 0$ marking the start of the damping layer, the damping increased until reaching a maximum at $x/R = 2.08$ and remained at maximum up to the boundary at $x/R = 2.5$. The source was located at $x/R = -20.42$. The two-point analysis to determine the propagating mode amplitudes in both directions within the duct was conducted at three axial locations along the duct. The results are shown in Table 4 and summarized as follows:

- The imposed source modes were the dominant modes propagating in the $+x$ direction. The other propagating modes have amplitudes 2 to 3 orders of magnitude less than the dominant mode. Thus, the source does not put any significant acoustic energy into any propagating modes other than the desired mode.
- The $(2,0)$ and $(2,1)$ propagating modes had amplitudes that were very close to the source amplitude near the source at $x/R = -20.17$, $|P^+_{20}| = 0.995|P^s_{20}|$ and $|P^+_{21}| = 0.991|P^s_{21}|$. The $(2,2)$ mode amplitude was slightly smaller than the source amplitude, $|P^+_{22}| = 0.966|P^s_{22}|$.
- The $+x$-direction propagating mode amplitudes vary slightly with axial location with a tendency to decrease away from the source.
- The damping layer produced minimal reflection of the incident mode and produced no significant scattering of acoustic energy into other propagating modes.
- While the changes in propagating mode amplitudes were noticeable, the mode power results show that the source power was transmitted into the dominant propagating mode with the $(2,0)$ and $(2,1)$ propagating modes showing no significant change in power while the $(2,2)$ propagating mode power showed a 0.3 dB to 0.5 dB loss in power from the imposed source sound power level.

Table 4: Propagating mode amplitudes and sound power levels in a long duct terminated by a damping layer boundary condition.

| | $x/R = -20.17$ | | | $x/R = -11.83$ | | | $x/R = -3.50$ | | |
|---|---|---|---|---|---|---|---|---|---|
| $(m,n)$ | $(2,0)$ | $(2,1)$ | $(2,2)$ | $(2,0)$ | $(2,1)$ | $(2,2)$ | $(2,0)$ | $(2,1)$ | $(2,2)$ |
| $\lvert P^s_{mn}\rvert$[a] | 1.4186 | 1.4186 | 1.4186 | 1.4186 | 1.4186 | 1.4186 | 1.4186 | 1.4186 | 1.4186 |
| $\lvert P^+_{mn}\rvert$ | 1.4118 | 1.4052 | 1.3704 | 1.4115 | 1.4036 | 1.3601 | 1.4122 | 1.4010 | 1.3408 |
| $\lvert P^-_{mn}\rvert$ | 0.0006 | 0.0010 | 0.0517 | 0.0003 | 0.0024 | 0.0500 | 0.0010 | 0.0006 | 0.0343 |
| $W^s_{mn}$[b] | 94.3 | 93.4 | 90.4 | 94.3 | 93.4 | 90.4 | 94.3 | 93.4 | 90.4 |
| $W^+_{mn}$ | 94.3 | 93.4 | 90.1 | 94.3 | 93.4 | 90.0 | 94.3 | 93.3 | 89.9 |
| other $\lvert P^+\rvert$[c] | 0.0012 | 0.0082 | 0.0120 | 0.0023 | 0.0150 | 0.0140 | 0.0020 | 0.0090 | 0.0140 |
| conv. $\lvert P^-\rvert$[d] | 0.0002 | 0.0015 | 0.0050 | 0.0002 | 0.0016 | 0.0051 | 0.0002 | 0.0016 | 0.0060 |

[a] Amplitudes $P$ are in Pa.

[b] Mode power in dB re. $10^{-12}$ watts.

[c] Maximum amplitude of other modes propagating away from the source.

[d] Maximum amplitude of other modes converted from incident mode at the boundary.

The loss in mode amplitude from the source into the acoustic field may be due to the structure of the grid and the shape of the mode. The circular grid in the duct interior contains grid singularities that result in lower order of accuracy numerical calculations near those points.[33] Near the source, this inaccuracy affects

how well the accurately defined source mode is transmitted into the computational domain. The result will depend on both the grid resolution and the mode shape. For the fixed grid at the source location, the effects show up as there is more variability in the mode shapes. Here, the mode shapes have fixed circumferential variation and as the radial mode index $n$ varies form 0 to 2, there is more radial variation. The low order accuracy has greater effect on modes with higher radial variation. Thus, the greater loss seen in the $(2,2)$ mode amplitude from the source to the acoustic field. This may be resolved by refining the grid near the source.

Table 5: Propagating mode amplitudes and sound power levels in a long duct terminated by the Giles boundary condition.[30,34]

| | $x/R=-22.67$ | | | $x/R=-14.33$ | | | $x/R=-6.00$ | | |
|---|---|---|---|---|---|---|---|---|---|
| $(m,n)$ | $(2,0)$ | $(2,1)$ | $(2,2)$ | $(2,0)$ | $(2,1)$ | $(2,2)$ | $(2,0)$ | $(2,1)$ | $(2,2)$ |
| $\lvert P^s_{mn}\rvert$[a] | 1.4186 | 1.4186 | 1.4186 | 1.4186 | 1.4186 | 1.4186 | 1.4186 | 1.4186 | 1.4186 |
| $\lvert P^+_{mn}\rvert$ | 1.4112 | 1.4056 | 1.5134 | 1.4110 | 1.4046 | 1.4938 | 1.4111 | 1.4005 | 1.4526 |
| $\lvert P^-_{mn}\rvert$ | 0.0299 | 0.1682 | 0.5859 | 0.0293 | 0.1718 | 0.5643 | 0.0299 | 0.1694 | 0.6111 |
| $\lvert P^-_{mn}\rvert/\lvert P^+_{mn}\rvert$ | 0.0212 | 0.1197 | 0.3871 | 0.0208 | 0.1223 | 0.3775 | 0.0212 | 0.1210 | 0.4207 |
| $W^s_{mn}$[b] | 94.3 | 93.4 | 90.4 | 94.3 | 93.4 | 90.4 | 94.3 | 93.4 | 90.4 |
| $W^+_{mn}$ | 94.3 | 93.4 | 90.9 | 94.3 | 93.4 | 90.8 | 94.3 | 93.3 | 90.6 |
| other $\lvert P^+\rvert$[c] | 0.0012 | 0.0080 | 0.0120 | 0.0022 | 0.0150 | 0.0140 | 0.0013 | 0.0090 | 0.0140 |
| conv. $\lvert P^-\rvert$[d] | 0.0004 | 0.0030 | 0.0067 | 0.0003 | 0.0027 | 0.0060 | 0.0002 | 0.0018 | 0.0051 |

[a] Amplitudes $P$ are in Pa.

[b] Mode power in dB re. $10^{-12}$ watts.

[c] Maximum amplitude of other modes propagating away from the source.

[d] Maximum amplitude of other modes converted from incident mode at the boundary.

The second test with modes propagating in a long duct had the Giles inflow boundary condition placed at the end and since there was no mean flow, the boundary condition only absorbed or reflected incoming acoustic waves. In this case, the origin of the $x$-axis was placed at the boundary resulting in a source location of $x/R=-22.92$. The results for the propagating mode amplitudes and sound power levels at three axial locations are shown in Table 5. Similarly to the damping layer results in Table 4, the acoustic energy of the source was imposed into the desired dominant propagating mode and no energy was converted into other propagating modes at the boundaries. However, the Giles boundary condition produced a significant reflected acoustic mode. As the approximate plane-wave angle of incidence increased from 16.4 degrees for the $(2,0)$ mode to 67.3 degrees for the $(2,2)$ mode, the magnitude of the reflection coefficient $|\Gamma_{mn}| = |P^-_{mn}|/|P^+_{mn}|$ increased from 0.0212 to 0.4207 as determined at $x/R=-6.00$. This results in the high level of $-x$-direction propagating mode amplitudes that subsequently affect the amplitudes of the modes propagating in the $+x$ direction. It was possible at this point to estimate a range of amplitudes for the $+x$-direction mode that would result from interaction with the reflected mode. Using a simplified model, the total $+x$-direction propagating mode amplitude is taken to be the sum of the initial propagating mode from the source end of the duct plus a second $+x$-direction propagating mode that results from two reflections, one from each end of the duct. A phase shift occurs as the acoustic mode propagates from one end of the duct to the other that affects the amplitude of the combined modes propagating in one direction. By setting the cosine of the phase shift to $\pm 1$, limiting values for the mode amplitude may be determined. The minimum and maximum amplitude for the total $+x$-direction propagating mode is given by

$$|P^+_{mn}| = |P^{1+}_{mn}| \left(1 \pm |\Gamma_{mn}|^2\right). \tag{13}$$

To get the range of amplitudes, $|P^{1+}_{mn}|$ is obtained from the $|P^+_{mn}|$ values at $x/R=-20.17$ in Table 4 and $|\Gamma_{mn}| = |P^-_{mn}|/|P^+_{mn}|$ is obtained from Table 5 at $x/R=-6.00$. The results are

$$\begin{aligned} 1.4112 \le |P^+_{20}| \le 1.4124 \qquad & |P^+_{20}| = 1.4112 \\ 1.3846 \le |P^+_{21}| \le 1.4258 \qquad & |P^+_{21}| = 1.4056 \\ 1.1279 \le |P^+_{22}| \le 1.6130 \qquad & |P^+_{22}| = 1.5134 \end{aligned}$$

The right side amplitudes are for the $+x$-direction modes near the source and as can be seen, they lie within the estimated range of possible mode amplitudes when reflections are occurring within the duct.

## VI. Concluding Remarks

The BASS code was used to compute the acoustic field within a circular duct generated by a source placed at one end of the duct. At the source plane, a higher-order acoustic mode was imposed for a mode that would propagate along the duct. The opposite end of the duct had a termination that was either open or closed. When the end was open, the computational domain extended outward from the duct and ended with a nonreflecting boundary condition. The geometry of the open end determined the physical behavior of the acoustic reflection back into the duct from the open end. Three shapes were used for the computational geometry: the infinite flange duct, the unflanged (thin) duct, and an intermediate flange (medium) duct. The closed end duct had either a damping layer or a computational, nonreflecting boundary condition.

The open end duct, computational solution was used to study the accuracy of the code to compute the proper physical interaction at the open end between a single, higher-order, incident mode and all the modes that return from the open end and propagate back towards the source. The relative change between these modes and the incident mode were used to determine the reflection matrix containing the reflection coefficient for the incident mode and the conversion coefficients for all the other propagating modes created from the incident mode at the open end. Theoretical reflection matrix values were computed for the infinite flanged and unflanged ducts and compared to the values determined from the computed data. The infinite flanged duct computed values were within 3% and the unflanged duct values within 4% of the theoretical reflection matrix values after grid refinement near the open end was performed. Since the reflection matrix values are relative to the incident mode amplitude, the absolute accuracy of the mode amplitude was not required to determine an accurate reflection matrix.

When the accuracy of the mode amplitude was checked for the single propagating mode imposed by the source, discrepancy in amplitude was noted. The study using the closed end duct showed:

1. The acoustic field contained only the incident mode propagating towards the closed end with the damping layer to suppress reflections. There were three propagating modes with increasing radial variation. The propagating mode amplitude within the duct was lower than the source amplitude with a larger discrepancy as the radial variation of the mode increased. It is suspected that grid singularities near the source inhibit transmission of the acoustic source into the field. A possible resolution is to refine the grid near the source. This is a subject for future work.

2. Placing the same computational nonreflecting boundary condition at both ends of the duct showed the actual level of reflection occurring with the higher-order modes propagating within the duct. Thus the boundary condition at the source, meant for allowing reflecting acoustic modes to leave the computational domain, was actually reflecting those modes back into the duct. Depending on their phase relationship, this reflected mode from the source plane would add or subtract from the initial incident mode and change the amplitude from that initially imposed by the source.

## Acknowledgment

The NASA Advanced Air Transport Technology Project of the Advanced Air Vehicles Program supported for this work.

## References

[1]Morse, P. M. and Ingard, K. U., *Theoretical Acoustics*, McGraw-Hill, 1968.

[2]Rayleigh, J. W. S., *The Theory of Sound*, Dover reprint 1945, New York, 1877.

[3]Morse, P. M., *Vibration and Sound*, McGraw-Hill, 2nd ed., 1948.

[4]Norris, A. N. and Sheng, I. C., "Acoustic Radiation from a Circular Pipe with an Infinite Flange," *J. Sound Vib.*, Vol. 135, No. 1, 1989, pp. 85–93.

[5]Zorumski, W. E., "Generalized Radiation Impedances and Reflection Coefficients of Circular and Annular Ducts," *J. Acoust. Soc. Am.*, Vol. 54, No. 6, 1973, pp. 1667–1673.

[6]Levine, H. and Schwinger, J., "On the Radiation of Sound from an Unflanged Circular Pipe," *Physical Review*, Vol. 73, No. 4, February 1948, pp. 383–406.

[7]Lansing, D. L., Drischler, J. A., and Pusey, C. G., "Radiation of Sound from an Unflanged Circular Duct with Flow," *79th Meeting of the Acoustical Society of America*, 1970.

[8]Rienstra, S. W., "Acoustic Radiation from a Semi-Infinite Annular Duct in a Uniform Subsonic Mean Flow," *J. Sound Vib.*, Vol. 94, No. 2, 1984, pp. 267–288.

[9]Cho, Y. C., "Rigorous Solutions for Sound Radiation from Circular Ducts with Hyperbolic Horns or Infinite Plane Baffle," *J. Sound Vib.*, Vol. 69, No. 3, 1980, pp. 405–425.

[10]Ando, Y., "On the Sound Radiation from Semi-Infinite Circular Pipe of Certain Wall Thickness," *Acustica*, Vol. 22, No. 4, 1969, pp. 219–225.

[11]Eversman, W., "Theoretical Models for Duct Acoustic Propagation and Radiation," *Aeroacoustics of Flight Vehicles: Theory and Practice Volume 1: Noise Sources*, edited by H. H. Hubbard, NASA RP-1258, chap. 13, 1991.

[12]Envia, E., Wilson, A. G., and Huff, D. L., "Fan Noise: A Challenge to CAA," *International Journal of Computational Fluid Dynamics*, Vol. 18, No. 6, 2004, pp. 471–480.

[13]Iob, A., Arina, R., and Schipani, C., "Frequency-Domain Linearized Euler Model for Turbomachinery Noise Radiation Through Engine Exhaust," *AIAA J.*, Vol. 48, No. 4, April 2010, pp. 848–858.

[14]Tam, C. K. W. and Hardin, J. C., editors, *Second Computational Aeroacoustics (CAA) Workshop on Benchmark Problems*, NASA CP-3352, 1997.

[15]Astley, R. J., "Wave Envelope and Infinite Elements for Acoustical Radiation," *Int. J. Num. Meth. Fluids*, Vol. 3, 1983, pp. 507–526.

[16]Meyer, H. D., "Effect of Inlet Reflections on Fan Noise Radiation," *AIAA J.*, Vol. 34, No. 9, 1996, pp. 1771–1777.

[17]Nallasamy, M., Sutliff, D. L., and Heidelberg, L. J., "Propagation of Spinning Acoustic Modes in Turbofan Exhaust Ducts," *J. Prop. Power*, Vol. 16, No. 5, September 2000, pp. 736–743.

[18]Dahl, M. D., Hixon, R., and Sutliff, D. L., "Further Development of Rotating Rake Mode Measurement Data Analysis," AIAA Paper No. 2013-2246, 2013.

[19]Nallasamy, M., Hixon, R., and Sawyer, S., "Solution of Unsteady Euler Equations: Gust-Cascade Interaction Tones," *Computers and Fluids*, Vol. 36, 2007, pp. 724–741.

[20]Hixon, R., Nallasamy, M., and Sawyer, S., "Progress Towards the Prediction of Turbomachinery Noise Using Computational Aeroacoustics," Paper IN06-119, Inter-Noise, December 2006.

[21]Hixon, R., Golubev, V. V., Mankbadi, R. R., Scott, J. R., Sawyer, S., and Nallasamy, M., "Application of a Nonlinear Computational Aeroacoustics Code to the Gust-Airfoil Problem," *AIAA J.*, Vol. 44, 2006, pp. 323–328.

[22]Hixon, R., Nallasamy, M., Sawyer, S., and Dyson, R., "Comparison of Numerical Schemes for a Realistic Computational Aeroacoustics Problem," *Int. J. of Aeroacoustics*, Vol. 3, 2004, pp. 379–397.

[23]Sawyer, S., Nallasamy, M., Hixon, R., and Dyson, R. W., "A Computational Aeroacoustic Prediction of Discrete-Frequency Rotor-Stator Interaction Noise: A Linear Theory Analysis," *Int. J. of Aeroacoustics*, Vol. 3, 2004, pp. 67–86.

[24]Hixon, R., Nallasamy, M., and Sawyer, S., "Parallization Strategy for an Explicit Computational Aeroacoustics Code," AIAA Paper No. 2002-2583, 2002.

[25]Snir, M., Otto, S., Huss-Lederman, S., Walker, D., and Dongarra, J., *MPI - The Complete Reference*, The MIT Press, Cambridge, Mass., 1998.

[26]Allampalli, V., Hixon, R., Nallasamy, M., and Sawyer, S., "High-Accuracy Large-Step Explicit Runge-Kutta (HALE-RK) Schemes for Computational Aeroacoustics," *J. Comp. Physics*, Vol. 228, No. 10, 2009, pp. 3837–3850.

[27]Hixon, R., Bhate, D., Nallasamy, M., and Sawyer, S., "Shock-Capturing Dissipation Schemes for Computational Aeroacoustics," AIAA Paper No. 2006-2413, May 2006.

[28]Kennedy, C. A. and Carpenter, M. H., "Several New Numerical Methods for Compressible Shear-Layer Simulations," *Appl. Num. Math.*, Vol. 14, 1994, pp. 397–433.

[29]Tam, C. K. W. and Webb, J. C., "Dispersion-Relation-Preserving Finite Difference Schemes for Computational Acoustics," *J. Comp. Physics*, Vol. 107, No. 2, 1993, pp. 262–281.

[30]Giles, M. B., "Nonreflecting Boundary Conditions for Euler Equation Calculations," *AIAA J.*, Vol. 28, 1990, pp. 2050–2058.

[31]GridPro/az3000, Program Development Company, White Plains, NY, 1993–2010.

[32]Dahl, M. D. and Sutliff, D. L., "Analysis of Dual Rotating Rake Data from the NASA Glenn Advanced Noise Control Fan Duct with Artificial Sources," AIAA Paper No. 2014-3316, 2014.

[33]Hixon, R., Nallasamy, M., and Sawyer, S., "Effect of Grid Singularities on the Solution Accuracy of a CAA Code," AIAA Paper No. 2003-0879, 2003.

[34]Mansouri, N., Hixon, R., and Ingraham, D., "Verification of the Accuracy of Non-reflecting Boundary Conditions Using an Analytical Method," AIAA Paper No. 2012-2062, 2012.

[35]Åbom, M., "Modal Decomposition in Ducts Based on Transfer Function Measurements Between Microphone Pairs," *J. Sound Vib.*, Vol. 135, No. 1, 1989, pp. 95–114.

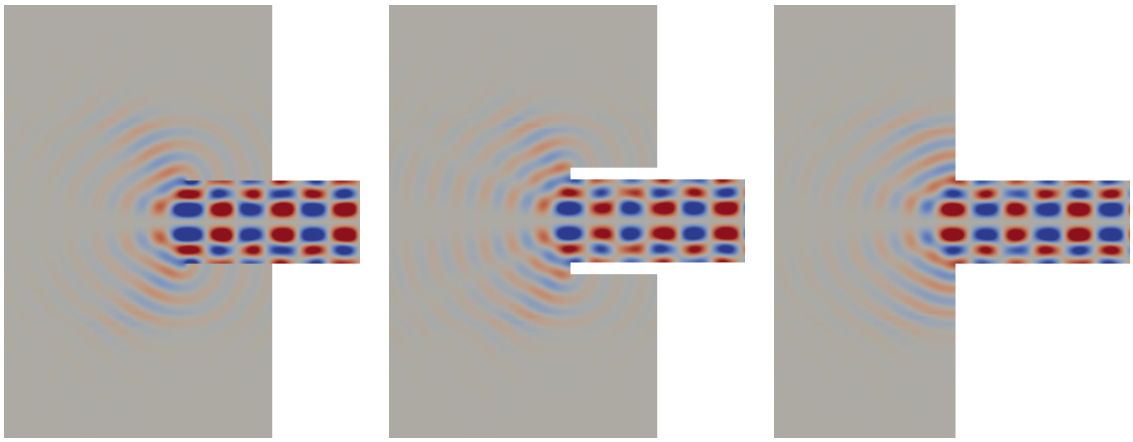

(a) Unflanged (thin) duct (b) Medium flanged duct (c) Infinite flanged duct

Figure 1: Computational examples for the (2,2) mode propagating in a duct with various open end configurations.

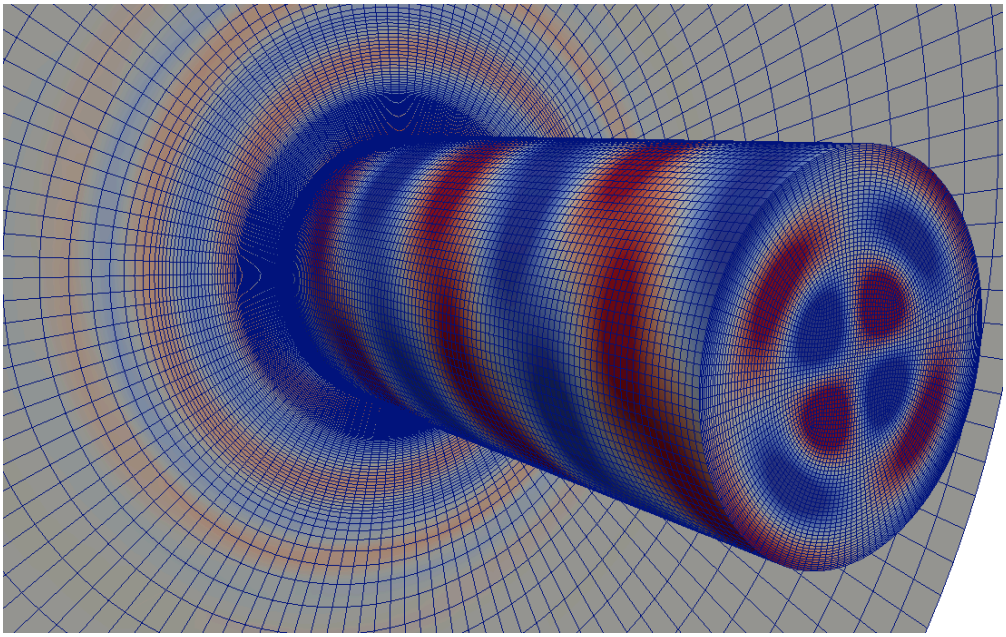

Figure 2: Outer surface grid for a circular duct with an infinite flange at the open end. Pressure contours are shown on the surface for propagating (2,2) mode.

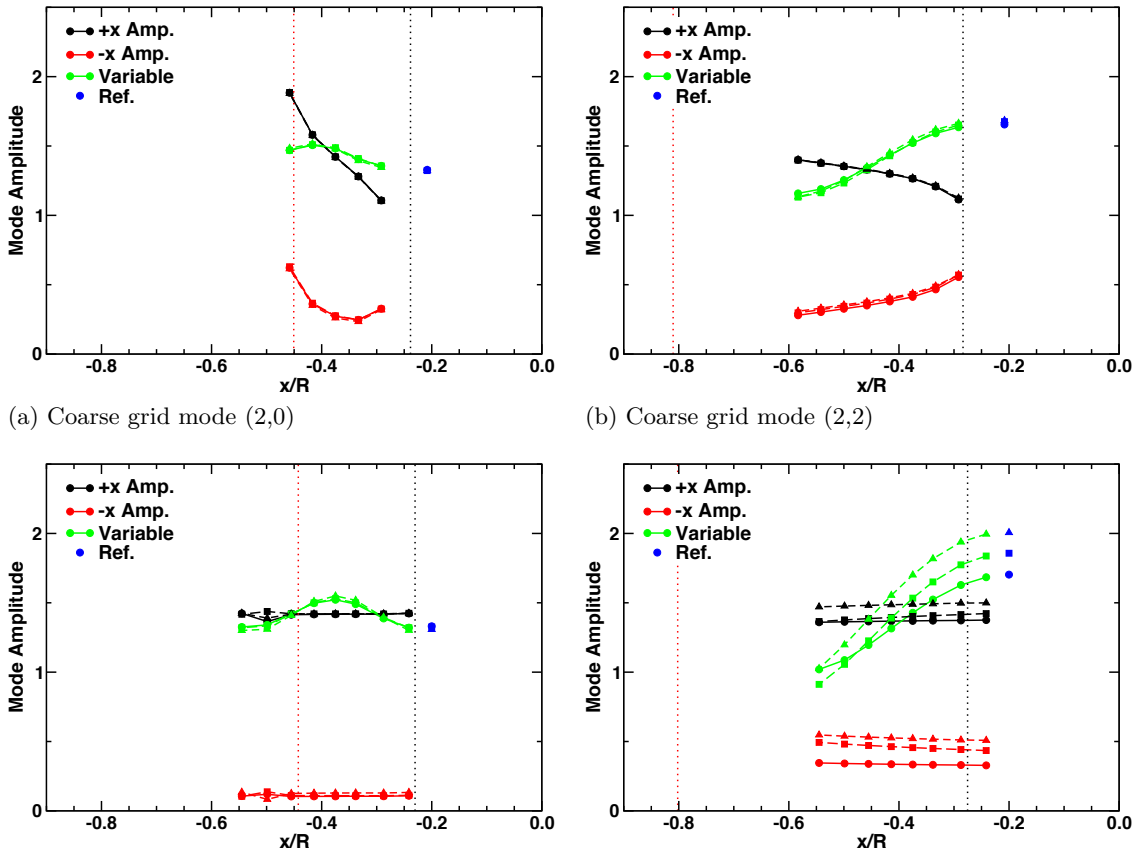


(a) Coarse grid mode (2,0)

(b) Coarse grid mode (2,2)

(c) Medium grid mode (2,0)

(d) Medium grid mode (2,2)

Figure 3: Comparison of one-point and two-point analyses for mode amplitude using BASS computed data with different open end conditions. 960 Hz. Unflanged (thin) duct (triangle, dashed line); Medium flanged duct (square, long dashed line); Infinite flanged duct (circle, solid line). Vertical dotted lines are practical limits for valid two-point analysis.[35]

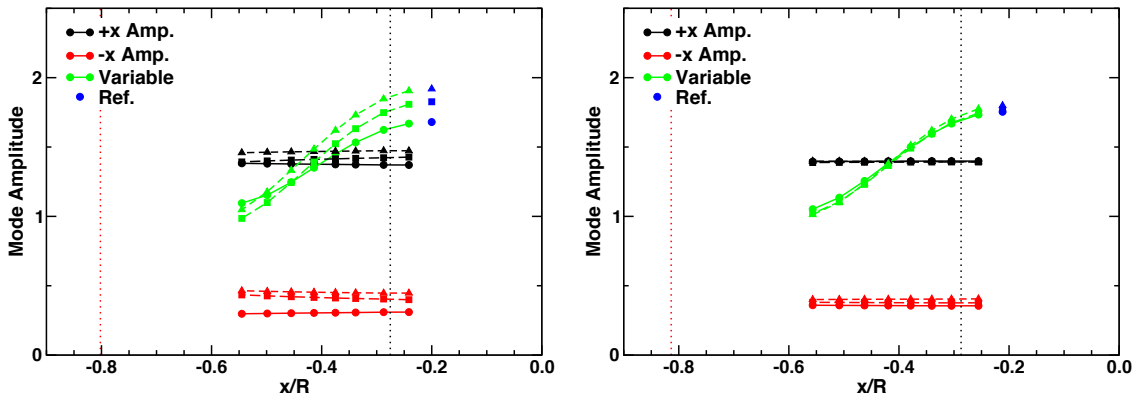


(a) Medium grid mode (2,2) longer time

(b) Fine grid mode (2,2)

Figure 4: Comparison of one-point and two-point analyses for mode amplitude using BASS computed data with different open end conditions. 960 Hz. Unflanged (thin) duct (triangle, dashed line); Medium flanged duct (square, long dashed line); Infinite flanged duct (circle, solid line). Vertical dotted lines are practical limits for valid two-point analysis.[35]

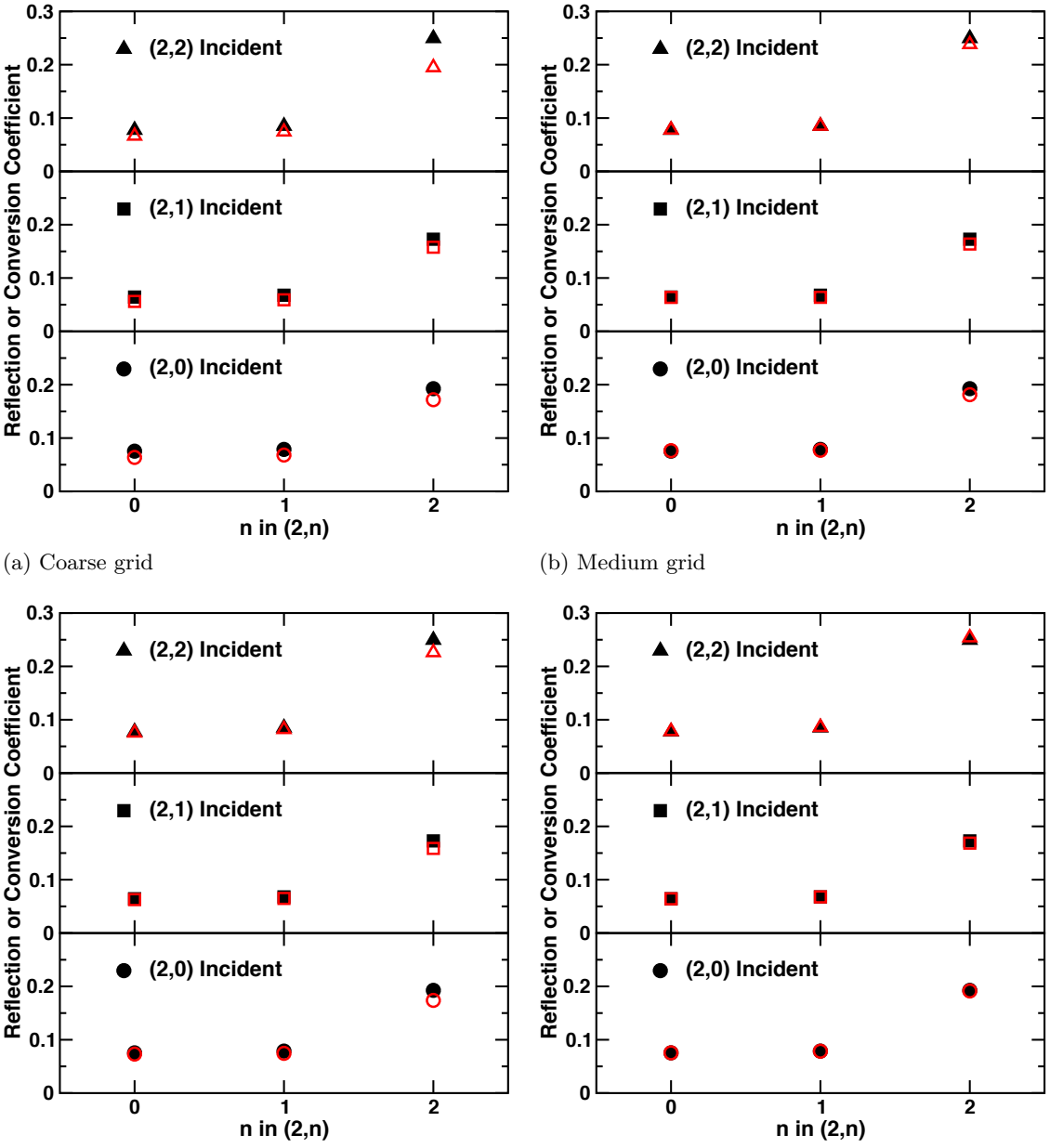


(a) Coarse grid

(b) Medium grid

(c) Medium grid longer time

(d) Fine grid

Figure 5: Infinite flanged duct reflection and conversion coefficients for the single incident mode indicated in the legend. Solid black symbols are theory results.[5] Open red symbols are results from BASS calculations.

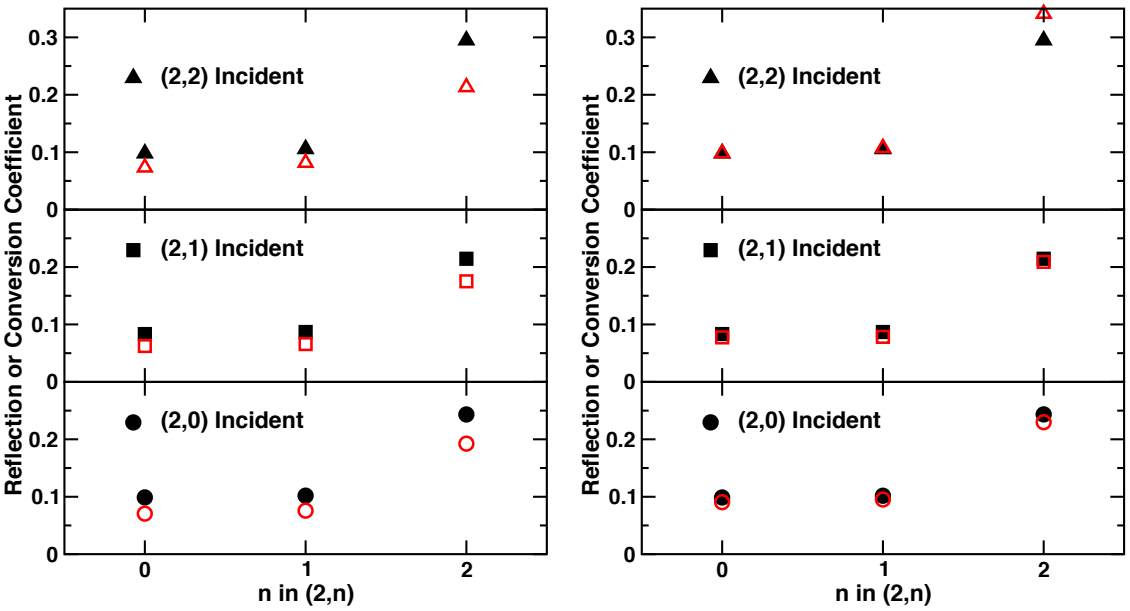


(a) Coarse grid

(b) Medium grid

(c) Medium grid longer time

(d) Fine grid

Figure 6: Unflanged (thin) duct reflection and conversion coefficients for the single incident mode indicated in the legend. Solid black symbols are theory results.[8] Open red symbols are results from BASS calculations.

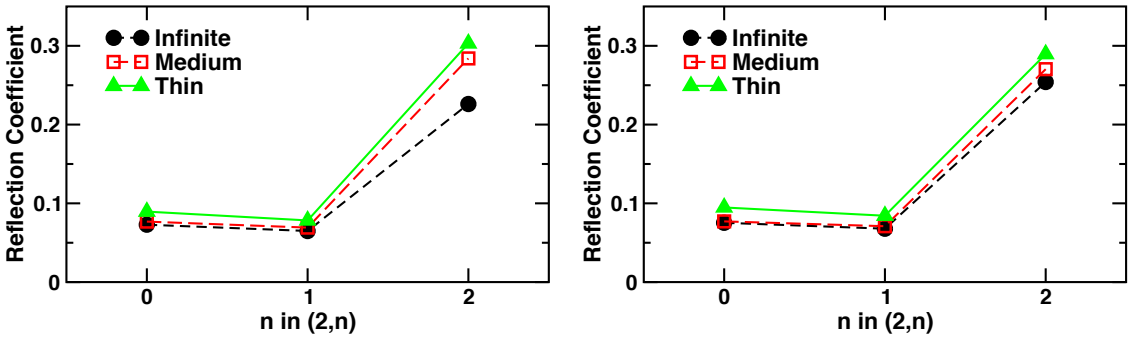


(a) Medium grid longer time

(b) Fine grid

Figure 7: Comparison of reflection coefficients for the indicated single incident mode for the infinite flanged duct, the medium flanged duct, and the unflanged (thin) duct.